The Astrophysical Journal, 975:167 (13pp), 2024 November 10 https://doi.org/10.3847/1538-4357/ad79f7

Revisiting the Vertical Distribution of H I Absorbing Clouds in the Solar Neighborhood. II. Constraints from a Large Catalog of 21 cm Absorption Observations at High Galactic Latitudes

Daniel R. Rybarczyk[1], Trey V. Wenger[1], and Snežana Stanimirović[2]
[1] NSF Astronomy & Astrophysics Postdoctoral Fellow, Department of Astronomy, University of Wisconsin–Madison, 475 N. Charter St., Madison, WI 53703, USA; rybarczyk@astro.wisc.edu
[2] Department of Astronomy, University of Wisconsin–Madison, 475 N. Charter St., Madison, WI 53703, USA
Received 2024 August 5; revised 2024 September 10; accepted 2024 September 10; published 2024 October 31

Abstract

The cold neutral medium (CNM) is where neutral atomic hydrogen (H I) is converted into molecular clouds, so the structure and kinematics of the CNM are key drivers of galaxy evolution. Here we provide new constraints on the vertical distribution of the CNM using the recently developed `kinematic_scaleheight` software package and a large catalog of sensitive H I absorption observations. We estimate the thickness of the CNM in the solar neighborhood to be $\sigma_z \sim 50$–90 pc, assuming a Gaussian vertical distribution. This is a factor of $\sim$2 smaller than typically assumed, indicating that the thickness of the CNM in the solar neighborhood is similar to that found in the inner Galaxy, consistent with recent simulation results. If we consider only structures with H I optical depths $\tau > 0.1$ or column densities $N(\mathrm{H\,I}) > 10^{19.5}\,\mathrm{cm}^{-2}$, which recent work suggests are thresholds for molecule formation, we find $\sigma_z \sim 50$ pc. Meanwhile, for structures with $\tau < 0.1$ or column densities $N(\mathrm{H\,I}) < 10^{19.5}\,\mathrm{cm}^{-2}$, we find $\sigma_z \sim 120$ pc. These thicknesses are similar to those derived for the thin- and thick-disk molecular cloud populations traced by CO emission, possibly suggesting that cold H I and CO are well mixed. Approximately 20% of CNM structures are identified as outliers, with kinematics that are not well explained by Galactic rotation. We show that some of these CNM structures—perhaps representing intermediate-velocity clouds—are associated with the Local Bubble wall. We compare our results to recent observations and simulations, and we discuss their implications for the multiphase structure of the Milky Way's interstellar medium.

Unified Astronomy Thesaurus concepts: Interstellar atomic gas (833); Cold neutral medium (266); Neutral hydrogen clouds (1099); Interstellar dynamics (839); Milky Way disk (1050)

1. Introduction

Neutral atomic hydrogen (H I) is a key ingredient in galaxy evolution. H I plays a crucial role in the transition from hot ionized gas to cold molecular gas, thereby mediating star formation and stellar feedback processes (see reviews by J. M. Dickey & F. J. Lockman 1990; P. M. W. Kalberla & J. Kerp 2009; N. M. McClure-Griffiths et al. 2023, and references therein). The distribution and kinematics of H I set the stage for the formation of molecular clouds and stars. They are also, in turn, affected by feedback.

The balance of heating and cooling in galaxies implies that H I should exist in a multiphase medium, with a colder, denser phase (the cold neutral medium (CNM)) and a warmer, more diffuse phase (the warm neutral medium (WNM)) that are thermally stable and exist in a rough pressure equilibrium (e.g., C. F. McKee & J. P. Ostriker 1977). In the Milky Way, the CNM and WNM have been characterized through observations of the 21 cm transition of H I in emission and absorption (J. M. Dickey & F. J. Lockman 1990; P. M. W. Kalberla & J. Kerp 2009; N. M. McClure-Griffiths et al. 2023, and references therein). The distribution of atomic gas between the CNM and WNM is important because it impacts galaxy evolution. For example, recent work has revealed that only the coldest, optically thickest H I, all of which is in the CNM, is associated with the formation of most molecular gas (S. Stanimirović et al. 2014; H. Nguyen et al. 2019; D. R. Rybarczyk et al. 2022; A. Hafner et al. 2023; G. Park et al. 2023), consistent with theoretical expectations (e.g., P. F. Goldsmith et al. 2007). Characterizing the structure and kinematics of the CNM in the Milky Way is therefore essential to understanding the evolution of the Galactic interstellar medium (ISM).

Moreover, the structure of the multiphase ISM is shaped by myriad physical processes. In particular, the vertical structure of the ISM is set by a balance between the gravitational force and the pressure gradient, which itself is affected by thermal, turbulent, radiative, magnetic, cosmic-ray, and feedback processes in the ISM (e.g., E. N. Parker 1969; J. B. G. M. Bloemen 1987; A. Boulares & D. P. Cox 1990; F. J. Lockman & C. S. Gehman 1991; A. S. Hill et al. 2012). Observational constraints on the vertical distribution of the multiphase ISM are necessary to test models and simulations of galaxy evolution.

Yet characterizing the structure of multiphase H I in the Galaxy has remained difficult. For example, observations of H I absorption are needed to unambiguously detect the CNM, but such observations are limited to a relatively small number of sight lines in the direction of randomly distributed background radio continuum sources. J. Crovisier (1978) developed a novel statistical technique for inferring the vertical thickness of the CNM disk using the positions and radial velocities of a sample of H I structures identified in absorption. The observed velocity of an H I structure is a combination of Galactic rotation, the Sun's motion relative to the local standard of rest (LSR), and a

random component. J. Crovisier (1978) expressed the Galactic rotation component in terms of the mean displacement of H I structures from the plane in the vertical (z) direction, $\langle|z|\rangle$. Then, by minimizing the difference between the expected and observed radial velocities, they were able to constrain $\langle|z|\rangle$ (see Section 3). They applied this technique to H I absorption observations (ensuring that they probed just the CNM) at high Galactic latitudes ($|b| \gtrsim 10°$, where discrete spectral features in the absorption spectra can reliably be identified; e.g., C. E. Murray et al. 2017), tracing primarily local gas structures ($d \lesssim 1$ kpc). For their sample of ∼300 absorbing H I structures (J. Crovisier et al. 1978), they estimated $\langle|z|\rangle = (107 \pm 29)$pc. For a Gaussian distribution, this corresponds to standard deviation in the z-direction of $\sigma_z = 134 \pm 36$ pc.

However, this result was recently called into question when T. V. Wenger et al. (2024) identified an error made by J. Crovisier (1978). T. V. Wenger et al. (2024) showed that, for any sample of structures truncated in latitude (including the sample used by J. Crovisier 1978, with a threshold $|b| > 10°$), the quantity that J. Crovisier (1978) measured was not, in fact, the mean displacement of the vertical distribution, but was instead a ratio of higher moments of the vertical distribution. Since J. Crovisier (1978) (and later P. Belfort & J. Crovisier 1984) reported this quantity as the mean displacement, the vertical thickness of the CNM in the solar neighborhood was overestimated. T. V. Wenger et al. (2024) developed an updated approach that accounts for distributions that are truncated in latitude. Using the same sample as J. Crovisier (1978), they found $\sigma_z = 61.7^{+9.6}_{-9.0}$ pc (assuming a Gaussian distribution), a factor of ∼2 lower than the reported J. Crovisier (1978) result.

Meanwhile, other approaches have been used to measure the thickness of the CNM at different Galactocentric radii. J. M. Dickey et al. (2009) used observations of H I absorption from three Galactic plane surveys (A. R. Taylor et al. 2003; N. M. McClure-Griffiths et al. 2005; J. M. Stil et al. 2006) to estimate the thickness of the CNM in the outer Galaxy, and J. M. Dickey et al. (2022) used observations of H I absorption from the Australian Square Kilometre Array Pathfinder (ASKAP; A. W. Hotan et al. 2021) to estimate the thickness of the CNM in the inner Galaxy. These projects characterized absorption at discrete Galactocentric radii (derived from the kinematics) rather than from discrete absorbing components, as the spectra in the plane are too complex for reliable Gaussian decomposition. In the inner Galaxy ($R \sim 2.8$–3.7 kpc), J. M. Dickey et al. (2022) found a CNM thickness of $\sigma_z \sim 50$–90 pc. At the solar circle (taken on the far side of the Galaxy, at a distance of 15.6 kpc), they estimated $\sigma_z = 160$ pc. In the outer Galaxy (from $R \sim 8.5$ to 25 pc), J. M. Dickey et al. (2009) found that the CNM had a thickness $\sigma_z \sim 170$–300 pc (see their Figure 7), showing the flaring of the disk beyond the solar circle. They found that the thickness of the CNM at these radii was comparable to the thickness of the WNM.

N. M. McClure-Griffiths et al. (2023) summarized the previous estimates of the CNM thickness as a function of Galactocentric radius (their Figure 11), showing a gradual rise in the CNM thickness from the inner to the outer Galaxy, similar to the trends seen for the WNM (E. S. Levine et al. 2006; P. M. W. Kalberla & J. Kerp 2009) and for the molecular gas (M. Heyer & T. M. Dame 2015, and references therein). They noted that this picture is consistent with expectations given the higher pressure in the inner Galaxy. However, when the CNM thickness in the solar neighborhood value is updated from the J. Crovisier (1978) result to the new result from T. V. Wenger et al. (2024), a different picture emerges. In contrast to the paradigm where the CNM thickness increases with increasing Galactocentric radius, this new result suggests that the thickness of the CNM in the solar neighborhood is actually comparable to that found in the inner Galaxy, at a Galactocentric radius of ∼3 kpc (J. M. Dickey et al. 2022).

Here we extend the work done by T. V. Wenger et al. (2024) by applying the `kinematic_scalehieght` code they developed (T. V. Wenger 2024) to a large catalog of high-latitude H I absorption observations compiled by N. M. McClure-Griffiths et al. (2023), the BIGHICAT (Section 2). Besides refining the method developed by J. Crovisier (1978) for observations truncated in latitude, T. V. Wenger et al. (2024) further developed two new Bayesian models that use Markov Chain Monte Carlo (MCMC) methods to constrain the thickness of the disk in a more reliable way (Section 3). In Section 4, we derive the vertical thickness of the CNM disk using each of these methods on different samples of the BIGHICAT. We present not only new estimates of the vertical thickness of the CNM but also new estimates of the cloud-to-cloud velocity dispersion and constraints on the solar motion with respect to the LSR. We also briefly investigate the properties of absorbing features with anomalous velocities that are identified as outliers. In Section 5, we discuss our results in the context of previous estimates of the CNM disk thickness, as well as recent galaxy-scale simulations of the multiphase ISM. Finally, we present our conclusions in Section 6.

2. Data

N. M. McClure-Griffiths et al. (2023) compiled H I absorption data from seven 21 cm line surveys—the Millennium Arecibo 21 cm Absorption-Line Survey with the Arecibo Observatory (C. Heiles & T. H. Troland 2003b, 2003a), a high-latitude survey with the Giant Metrewave Radio Telescope (R. Mohan et al. 2004a, 2004b), a survey in the direction of the Perseus molecular cloud with Arecibo (S. Stanimirović et al. 2014), the 21 cm Spectral Line Observations of Neutral Gas with the Karl G. Jansky Very Large Array (VLA) (21-SPONGE; C. E. Murray et al. 2015, 2018), a survey of HI absorption in the direction of the Riegel-Crutcher cloud (H. Dénes et al. 2018), a survey of H I absorption in the direction of five giant molecular clouds (Taurus, California, Rosette, Mon OB1, and NGC 2264) with Arecibo (H. Nguyen et al. 2019), and the Measuring Absorption by Cold Hydrogen (MACH) survey with the VLA (C. E. Murray et al. 2021)—into a catalog called the BIGHICAT. The BIGHICAT comprises 1223 unique Gaussian components identified in H I absorption.

Here we consider the 768 BIGHICAT features identified at Galactic latitudes $|b| > 5°$. Following J. Crovisier (1978), we focus only on higher latitudes because the absorption spectra are simpler and can be more reliably decomposed into Gaussian components (e.g., C. E. Murray et al. 2017). Moreover, the thickness of the H I disk is thought to be a function of Galactocentric radius (e.g., E. S. Levine et al. 2006; P. M. W. Kalberla & J. Kerp 2009). Focusing on high-latitude observations allows us to trace primarily local structures ($d < 2$ kpc), whereas features detected closer to the plane may probe different regions of the Galaxy. In Figure 1, we show the distribution of the optical depths (τ), H I column densities (N

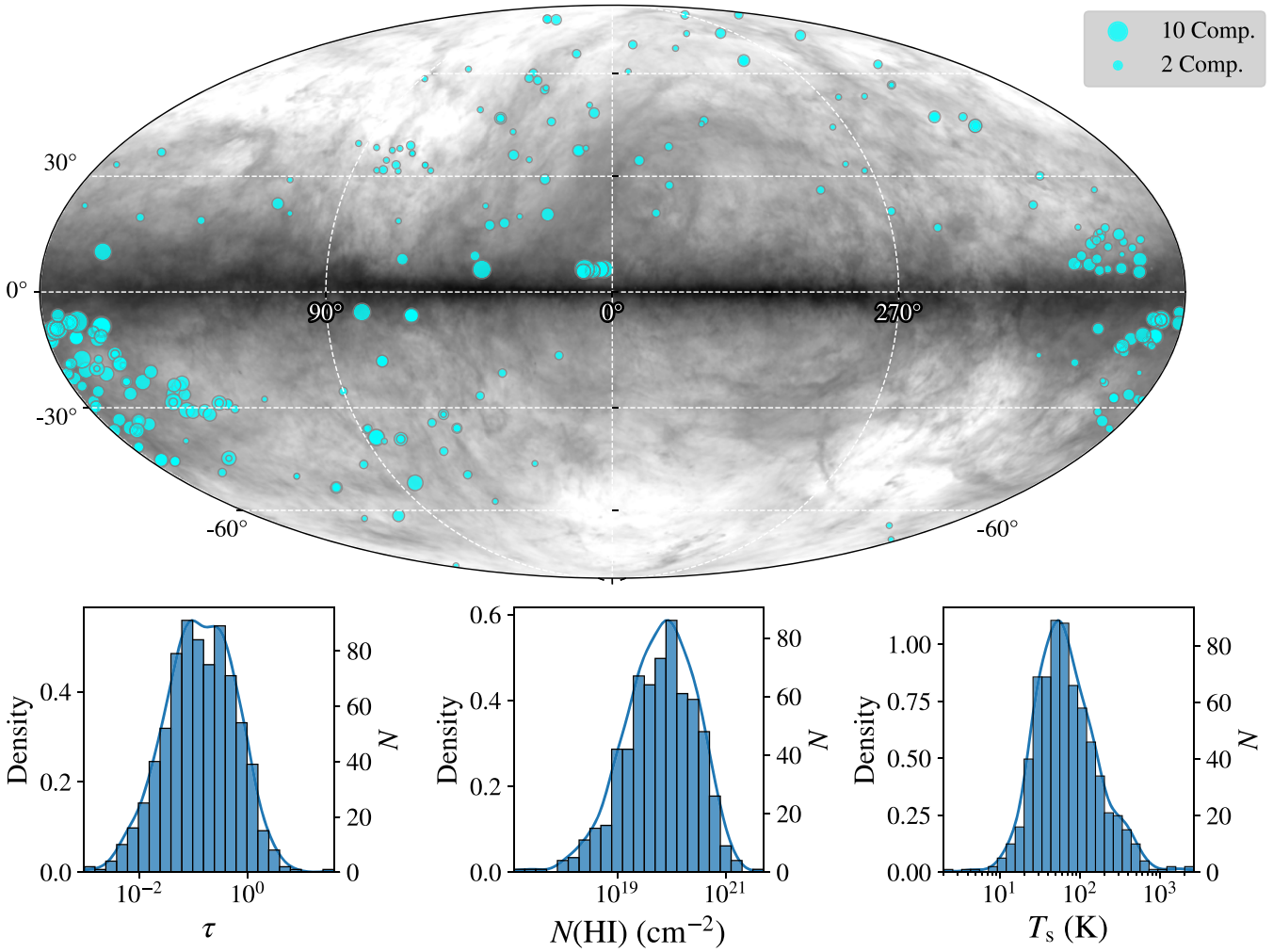

Figure 1. Top: the positions of the BIGHICAT background sources at $|b| > 5°$, sized according to the number of components detected along each line of sight. The background is a Mollweide projection of H I emission integrated from −75 to +75 km s^{-1} (HI4PI Collaboration et al. 2016). Bottom: distribution of H I optical depth (left), H I column density (middle), and H I spin temperature (right) for structures in the BIGHICAT sample with $|b| > 5°$. In each panel, a histogram is shown with the kernel density estimation overlaid.

(H I)), and spin temperatures[3] (T_S) for the total sample. While the optical depth is measured for all components, only 87% of components have estimated spin temperatures and 83% of components have estimated column densities (see N. M. McClure-Griffiths et al. 2023 for discussion of the BIGHICAT construction and completeness).

3. Methods

We apply the `kinematic_scaleheight` code (T. V. Wenger 2024) developed by T. V. Wenger et al. (2024) to different subsamples of the BIGHICAT to characterize the vertical distribution of the CNM in the solar neighborhood. As in J. Crovisier (1978), this algorithm infers the mean vertical displacement by comparing the observed radial velocities of CNM clouds with the expected radial velocities,

$$V_{\rm LSR} = V_{\odot,\rm LSR}(l, b) + V_{\rm rot}(d, l, b) + V_t, \quad (1)$$

where $V_{\odot,\rm LSR}$ is the line-of-sight velocity of the Sun with respect to the LSR, $V_{\rm rot}$ is the line-of-sight velocity of the cloud due to Galactic rotation, and V_t is the line-of-sight velocity of the cloud due to random cloud-to-cloud motions. J. Crovisier (1978) expressed $V_{\rm rot}$ in terms of $\langle|z|\rangle$ and used a least-squares method to infer $\langle|z|\rangle$. However, T. V. Wenger et al. (2024) identified an error in their method, showing that the quantity that J. Crovisier (1978) measured was not $\langle|z|\rangle$, but instead a ratio of the higher moments of the z distribution. The `kinematic_scaleheight` code implements a least-squares method that infers this moment ratio (which, contrary to the assumption of J. Crovisier (1978), is not equal to $\langle|z|\rangle$). The `kinematic_scaleheight` code also implements two Bayesian models—the "moment ratio" method parameterized in terms of $\langle|z|^3\rangle/\langle|z|^2\rangle$ and the "shape" method parameterized in terms of a shape parameter (which assumes a shape of the vertical distribution)—that use MCMC methods to infer the posterior distributions of model parameters. Both of the MCMC methods also identify outliers and infer model parameters only for the nonoutlying data.

When applying the `kinematic_scaleheight` code to the BIGHICAT, we must consider whether the distribution of background sources could be biasing our results. The BIGHICAT background sources are not randomly distributed across

[3] The spin temperature of H I is the excitation temperature for the 21 cm hyperfine transition.

Table 1
Estimates of σ_z from the `kinematic_scaleheight` Code for Different Samples of BIGHICAT Components

Sample	N	$\sigma_{z,\mathrm{ls}}$ (pc)	$\sigma_{z,\mathrm{MR}}$ (pc)	$\sigma_{z,\mathrm{shape}}$ (pc)
$\lvert b\rvert > 5°$	768	98.9 ± 7.6	74.3 ± 7.8	75.0 ± 8.0
$\tau > 0.1$, $\lvert b\rvert > 5°$	431	81.0 ± 7.1	58.7 ± 7.0	59.2 ± 7.0
$\tau < 0.1$, $\lvert b\rvert > 5°$	336	123.5 ± 14.7	119.8 ± 15.5	122.4 ± 15.3
$N(\mathrm{H\,I}) > 10^{19.5}$ cm^{-2}, $\lvert b\rvert > 5°$	429	71.0 ± 7.5	47.7 ± 6.3	48.0 ± 6.4
$N(\mathrm{H\,I}) < 10^{19.5}$ cm^{-2}, $\lvert b\rvert > 5°$	216	152.7 ± 19.9	127.2 ± 22.9	133.7 ± 23.6
$T_s < 80$ K, $\lvert b\rvert > 5°$	423	110.9 ± 11.8	61.4 ± 9.8	62.8 ± 9.8
$T_s > 80$ K, $\lvert b\rvert > 5°$	257	74.9 ± 11.4	57.5 ± 11.2	59.0 ± 11.4
$T_s < 80$ K, $\tau > 0.1$, $\lvert b\rvert > 5°$	296	80.4 ± 10.0	46.0 ± 7.2	46.5 ± 7.3
$T_s > 80$ K, $\tau < 0.1$, $\lvert b\rvert > 5°$	171	115.9 ± 18.0	107.5 ± 21.3	111.9 ± 20.9

Notes. The first column describes each subsample. The second column lists the number of unique BIGHICAT components, N, belonging to each subsample. The third column lists the vertical thickness derived using the `kinematic_scaleheight` least-squares method, $\sigma_{z,\mathrm{ls}}$. The fourth column lists the vertical thickness derived using the `kinematic_scaleheight` moment ratio method, $\sigma_{z,\mathrm{MR}}$. The fifth column lists the vertical thickness derived using the `kinematic_scaleheight` shape method, $\sigma_{z,\mathrm{shape}}$. In all cases, we assume a Gaussian vertical distribution.

the sky—the fractions of components at $\lvert b\rvert > 5°$ in the first, second, third, and fourth Galactic quadrants are 26.6%, 43.1%, 3.6%, and 26.7%, respectively. Meanwhile, 49.0% of those components have latitudes $5° \leqslant \lvert b\rvert \leqslant 20°$, 25.7% have latitudes $20° < \lvert b\rvert \leqslant 35°$, 17.1% have latitudes $35° < \lvert b\rvert \leqslant 50°$, and 8.3% have latitudes $\lvert b\rvert > 50°$. To test how this nonuniform sky coverage affects the fitting results, we apply the fitting to synthetic populations of clouds with different values of σ_z. For each synthetic population of clouds, we apply the `kinematic_scaleheight` code to a subsample of 200 clouds (comparable to the smallest sample size in Table 1) drawn from the same longitude−latitude distribution as the BIGHICAT sample and to another subsample of 200 randomly selected clouds. For samples with $\sigma_z \leqslant 150$ pc, we find that the two Bayesian techniques converge on the correct solutions for σ_z, σ_v (see Section 4.2), $U_\odot$, $V_\odot$, and $W_\odot$ (within $\lesssim 2.5\sigma$) in all cases, regardless of the sky distribution of the clouds.[4] In Figure 2, we show swarm plots for the error in the derived parameters for the control (randomly distributed) samples and the samples drawn from the same distribution as the BIGHICAT. We specifically present results from the shape model, but the results for the two MCMC techniques are not statistically significantly different. We show results for 14 synthetic samples, each with different values of σ_z, ranging from 40 to 300 pc; points are colored according to the value of σ_z for each synthetic sample. These swarm plots show that (1) the nonrandom distribution of the clouds in the sample does not strongly bias our results and (2) for both the randomly and nonrandomly drawn samples the Bayesian methods converge on the correct solution. The only exception is that we tend to slightly underestimate σ_v, and this bias is slightly enhanced in the BIGHICAT distribution samples. For samples with $\sigma_z \lesssim 150$ pc (which we expect for the local CNM; e.g., J. M. Dickey et al. 2022; T. V. Wenger et al. 2024), this bias is $<3\sigma$, but for some samples with larger σ_z the bias is as high as $\sim 4\sigma$. We take the results of these tests as evidence that the distribution of the BIGHICAT background sources should not significantly impact our estimates of the CNM thickness in the solar neighborhood.

Finally, we argue that our results are unlikely to be affected by the presence of a Galactic lagging halo. While a z-dependent velocity lag could significantly bias the results (since both J. Crovisier 1978 and T. V. Wenger et al. 2024 ignore such a lag), typical velocity lags of H I in disk galaxies are approximately $-10\,\mathrm{km\,s^{-1}\,kpc^{-1}}$ (e.g., A. Marasco et al. 2019), and for the Milky Way in particular, A. Marasco & F. Fraternali (2011) found the lag to be $-15 \pm 4\,\mathrm{km\,s^{-1}\,kpc^{-1}}$. In Section 4, we find that most of the H I exists within approximately ± 100 pc of the plane, so we expect that any velocity offsets introduced by a lagging halo are significantly smaller than the cloud-to-cloud velocity dispersion of cold H I (see Section 4.2 and, e.g., J. Crovisier 1978; P. Belfort & J. Crovisier 1984; N. M. McClure-Griffiths & J. M. Dickey 2007; T. V. Wenger et al. 2024).

4. Results

4.1. The Thickness of the CNM in the Solar Neighborhood

In Table 1, we report the derived vertical thicknesses for different subsamples of the BIGHICAT sample. The results in Table 1 differ significantly between the different samples—the vertical distribution of H I is not the same for all samples of absorbing structures. Here we investigate how the thickness of the cold H I disk depends on the atomic gas properties. For consistency, we assume a Gaussian distribution[5] and report the standard deviation in the z-direction, σ_z. We report the fits from the updated least-squares method, the moment ratio method, and the shape method introduced by T. V. Wenger et al. (2024) ($\sigma_{z,\mathrm{ls}}$, $\sigma_{z,\mathrm{MR}}$, and $\sigma_{z,\mathrm{shape}}$, respectively). In all cases, $\sigma_{z,\mathrm{MR}}$ and $\sigma_{z,\mathrm{shape}}$ are consistent with each other, varying by $<0.2\sigma$. The estimates from the corrected least-squares method are higher than those from the moment ratio method and shape method by $\gtrsim 3\sigma$ in two out of nine cases, emphasizing the importance of the treatment of outliers in the two MCMC methods.

4.1.1. Optical Depth Dependence

The H I optical depth is proportional to the density of atomic hydrogen and inversely proportional to its spin temperature and velocity dispersion. Previous work has shown that most of the molecule formation in the diffuse ISM is associated with only the optically thickest H I, $\tau \gtrsim 0.1$ (S. Stanimirović et al. 2014; H. Nguyen et al. 2019; D. R. Rybarczyk et al. 2022; A. Hafner et al. 2023; G. Park et al. 2023).

In Table 1, we report that $\sigma_z = 59.2 \pm 7.0$ for the sample of BIGHICAT structures with $\tau \geqslant 0.1$, while $\sigma_z = 122.4 \pm 15.3$ for the sample of structures with $\tau < 0.1$. The estimate for the optically thicker sample is in good agreement with estimates for the thickness of the molecular gas disk at distances $\lesssim 2$ kpc from the Sun, $\sigma_z \approx 40$–70 pc (D. B. Sanders et al. 1984; D. A. Grabelsky et al. 1987; L. Bronfman et al. 1988;

[4] The results for the least-squares technique similarly converge to the correct solution (within 2.5σ) for $U_\odot$, $V_\odot$, and $W_\odot$ but sometimes overestimate σ_z and σ_v by a larger degree than the Bayesian methods.

[5] As in T. V. Wenger et al. (2024), we neither rule out nor strongly favor any of the three different shapes of the vertical distribution implemented by the kinematic_scalehieght code—Gaussian, exponential, or rectangular—using leave-one-out cross-validation (A. Vehtari et al. 2021).

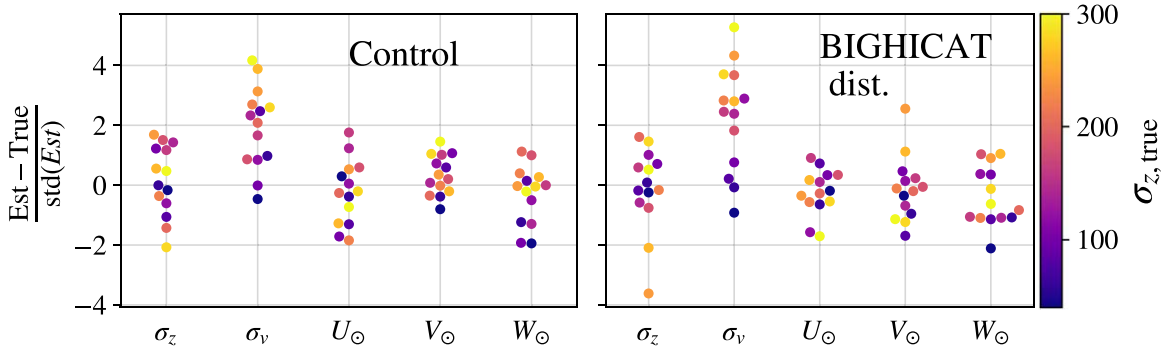

Figure 2. Swarm plots of the parameters derived for synthetic populations of clouds drawn randomly across the sky (left; "Control") and synthetic populations of clouds drawn from the same (ℓ, b) distribution as the BIGHICAT background sources (right; "BIGHICAT dist."). The x-axis indicates the variable (σ_z, σ_v, $U_\odot$, $V_\odot$, or $W_\odot$; small horizontal offsets are used to prevent points from overlapping), and the y-axis indicates the error in the estimated parameter, normalized by the uncertainty in the fit. We show results for 14 synthetic samples, each with different values of σ_z, ranging from 40 to 300 pc; points are colored according to the value of σ_z for each synthetic sample.

D. P. Clemens et al. 1988; S. Malhotra 1994; H. Nakanishi & Y. Sofue 2006). Meanwhile, the estimate for the optically thinner sample is closer to what is estimated for H I seen in emission. In the solar neighborhood, the thickness of the disk derived from H I emission observations is $\sigma_z \approx 110$–180 pc (E. Falgarone & J. Lequeux 1973; P. M. W. Kalberla & L. Dedes 2008; P. M. W. Kalberla & J. Kerp 2009). Many authors have used a two-component fit to account for the vertical distribution of the H I seen in emission, with $\sigma_{z,1} \approx 100$ pc and $\sigma_{z,2} \approx 240$ pc (F. J. Lockman et al. 1986; J. M. Dickey & F. J. Lockman 1990; F. J. Lockman & C. S. Gehman 1991). Our result for the $\tau < 0.1$ sample is similar to the thickness of the thinner of the two components in such models.

In Figure 3, we take a more fine-grained approach by considering six samples, each with ∼125 features, sorted by increasing optical depth. The thicknesses we measure for two samples comprising H I structures with $\tau < 0.1$ are both >100 pc, while the thicknesses we measure for the four samples comprising H I structures with $\tau > 0.1$ are all around $\sigma_z \approx 50$–70 pc. The optical depth threshold of 0.1 presented in Table 1 was motivated by the fact that this appears to be a necessary (but not sufficient) criterion for molecule formation in the diffuse ISM (H. Nguyen et al. 2019; D. R. Rybarczyk et al. 2022; A. Hafner et al. 2023; G. Park et al. 2023). Evidently, a similar threshold also delineates cold H I clouds in terms of their vertical distributions: the optically thicker sample is more tightly confined to the plane (intriguingly, in a vertical distribution similar to that of the molecular gas in the solar neighborhood), while the optically thinner sample has a wider distribution in the z-direction (closer to that derived from H I emission).

4.1.2. H I Column Density Dependence

The column density of an atomic gas structure is related to the density of the structure, $N(\mathrm{H\,I}) = \int n(\mathrm{H\,I})\, dl$, and indicates how well shielded the gas is (although this depends on the geometry of the gas structure). D. R. Rybarczyk et al. (2022) showed that diffuse molecular gas was associated only with CNM structures that had a column density $N(\mathrm{H\,I}) \gtrsim 10^{19.5}$. In Table 1, we report that $\sigma_z = 133.7 \pm 23.6$ for structures in the BIGHICAT with $N(\mathrm{H\,I}) < 10^{19.5}$ cm^{-2}, while $\sigma_z = 48.0 \pm 6.4$ for

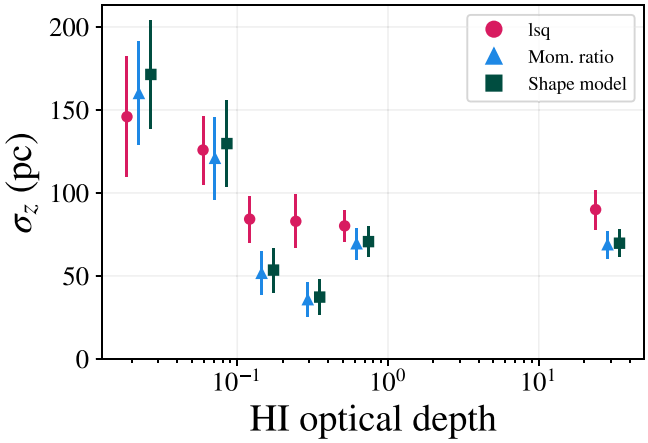

Figure 3. Fits to σ_z for six subsamples of the BIGHICAT sorted by H I optical depth. Results for the updated least-squares, the moment ratio, and the shape methods implemented by the `kinematic_scaleheight` code are shown. The x-axis value for each point is placed near the center of the optical depth range of the corresponding subsample; the x-axis value for each method is slightly offset for clarity.

the structures with $N(\mathrm{H\,I}) > 10^{19.5}$ cm^{-2}. These results are consistent with the vertical distributions inferred for the $\tau < 0.1$ and $\tau > 0.1$ samples, respectively. The H I optical depth and H I column density are well correlated, and 74% of structures with $N(\mathrm{H\,I}) > 10^{19.5}$ cm^{-2} have $\tau > 0.1$, so it is unsurprising that the results are in good agreement with the optical depth results discussed above.

We take a more fine-grained look at the dependence of σ_z on H I column density in Figure 4. We sort the BIGHICAT by H I column density and consider six samples, each with ∼105 structures. Figure 4 shows that the thicknesses we measure for two samples comprising H I structures with $N(\mathrm{H\,I}) \lesssim 10^{20}$ cm^{-2} are both >100 pc, while the thicknesses we measure for the four samples comprising H I structures with $N(\mathrm{H\,I}) \lesssim 10^{20}$ cm^{-2} are all around $\sigma_z \approx 50$–70 pc. These results are very similar to those we found for the H I optical depth above, but this is, again, unsurprising since correlation between the H I optical depth and H I column density suggests that the two analyses are probing similar structures. Here we find that a threshold column density of $\sim 10^{20}$ cm^{-2} delineates the thinner and thicker H I populations discussed above.

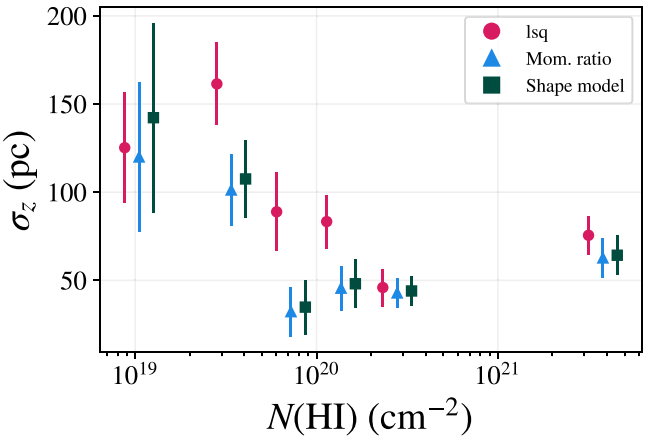

Figure 4. Same as Figure 3, but for six subsamples of the BIGHICAT sorted by H I column density.

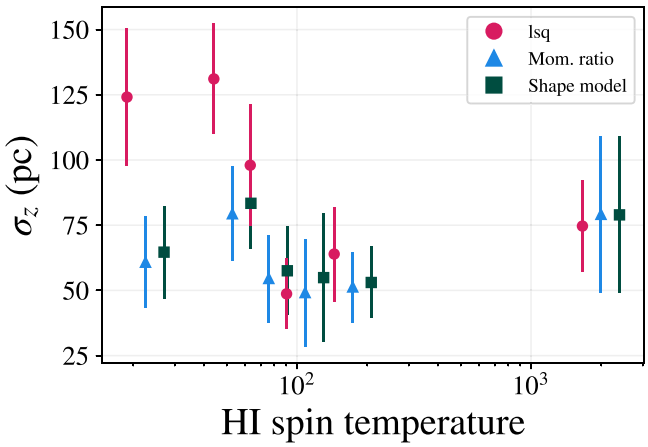

Figure 5. Same as Figure 3, but for six subsamples of the BIGHICAT sorted by H I spin temperature.

4.1.3. Temperature Dependence

The spin temperature of H I is approximately equal to its kinetic temperature in the high-density CNM, where the 21 cm transition is thermalized by collisions with electrons, ions, and other hydrogen atoms. In the high-latitude BIGHICAT sample used here, 91% of features have $T_S < 250$ K and only 4 of the 680 measured spin temperatures have $T_S > 1000$ K. We therefore treat T_S in this sample as a reasonable estimate of the kinetic temperature, allowing us to investigate how the thickness of the disk depends on the temperature of the atomic gas. In the solar neighborhood, the CNM is expected to have temperatures $T_S \lesssim 250$ K, while the WNM is expected to have temperatures $T_S \gtrsim 4000$ K (e.g., M. G. Wolfire et al. 2003). Gas in the intermediate-temperature regime belongs to the unstable neutral medium, which is thermally unstable but composes about 20% of the total mass of H I in the Milky Way (C. E. Murray et al. 2018). Comparisons of H I absorption measurements to molecular gas observations have confirmed that only the coldest atomic gas is associated with molecule formation—D. R. Rybarczyk et al. (2022) found molecular gas associated only with structures that had $T_S \lesssim 80$ K, while G. Park et al. (2023) found a threshold of $T_S \lesssim 200$ K and A. Hafner et al. (2023) found $T_S \lesssim 140$ K.

In Table 1, we report that $\sigma_z = 59.0 \pm 11.4$ for the sample of BIGHICAT structures with $T_S > 80$ K, where it is unlikely for H I to be associated with molecule formation (e.g., D. R. Rybarczyk et al. 2022). Meanwhile, for the sample of structures with $T_S < 80$ K, we find $\sigma_z = 62.8 \pm 9.8$. Whereas the optical depth and column density thresholds for molecule formation (H. Nguyen et al. 2019; D. R. Rybarczyk et al. 2022; A. Hafner et al. 2023; G. Park et al. 2023) seem to be associated with changes in the vertical structure of the H I, we do not see such a delineation associated with the temperature threshold. In Figure 5, we further divide the sample into six bins each with ~110 components sorted by increasing temperature. Again, we find $\sigma_z \approx 60$–80 pc in all samples, with no statistically significant variations between any of the six samples.

A. S. Hill et al. (2018) investigated the vertical distribution of gas as a function of temperature in 3D magnetohydrodynamic simulations of the multiphase ISM (M. K. R. Joung & M.-M. Mac Low 2006; M. R. Joung et al. 2009; A. S. Hill et al. 2012). Their Figure 6 suggests that the atomic gas at temperatures between $T \sim 20$ and 200 K is fairly uniformly distributed in the range 0 pc $\lesssim |z| \lesssim$ 100 pc. We note that 89% of the high-latitude BIGHICAT sample has $T_S < 200$ K.

In Table 1, we also consider the optical depth and spin temperature together, as both seem to be important to setting the conditions for molecule formation (e.g., D. R. Rybarczyk et al. 2022; A. Hafner et al. 2023; G. Park et al. 2023). We find that for structures with $T_S < 80$ K and $\tau > 0.1$—conditions necessary but not sufficient for the formation of diffuse molecular gas in the sample of D. R. Rybarczyk et al. (2022)—the measured thickness is $\sigma_z = 46.5 \pm 7.3$, while for structures with $T_S > 80$ K and $\tau < 0.1$ the measured thickness is $\sigma_z = 111.9 \pm 20.9$. These results are not significantly different from those where we considered only the optical depth threshold.

4.1.4. Comparison to Other Data Sets

In Figure 6, we re-create Figure 11 of N. M. McClure-Griffiths et al. (2023), which shows the thickness of the disk as a function of Galactocentric radius measured in H I emission (blue squares), H I absorption (orange diamonds), and CO emission (yellow squares). We overplot results from this work with magenta crosses. The thickness measured for the total high-latitude sample is shown as a dark-magenta cross, while those measured for the sample with $\tau > 0.1$ and $\tau < 0.1$ are showed as semitransparent magenta crossess (these values come from the first three columns of Table 1). The result from J. Crovisier (1978) is shown as an open diamond. As discussed above, the optically thicker sample has a thickness close to that measured for the molecular gas disk. The optically thinner sample is associated with a thicker disk, about halfway between the molecular gas disk and the disk measured in H I emission.

The exponential fit to the thickness of the H I disk is shown as a black line (interpolated as a gray line for $R < 5$ kpc), with a radial scale length of ~9.8 kpc (P. M. W. Kalberla et al. 2007; P. M. W. Kalberla & L. Dedes 2008). We further fit exponential functions to the CO (L. Bronfman et al. 1988; D. P. Clemens et al. 1988) and WNM (N. M. McClure-Griffiths et al. 2023), shown in yellow and blue, respectively. For the CO we find a radial scale length of 6.6 ± 0.6 kpc, while for the WNM we find a radial scale length of 9.4 ± 1.3 kpc. We do not find a good exponential fit for the CNM ($\chi^2 \gg 1$), which is reasonable if the thickness of the CNM is indeed constant for much of the Galaxy, as suggested by, e.g., R. J. Smith et al. (2023) (see Section 5). Nevertheless, it is worth noting the the

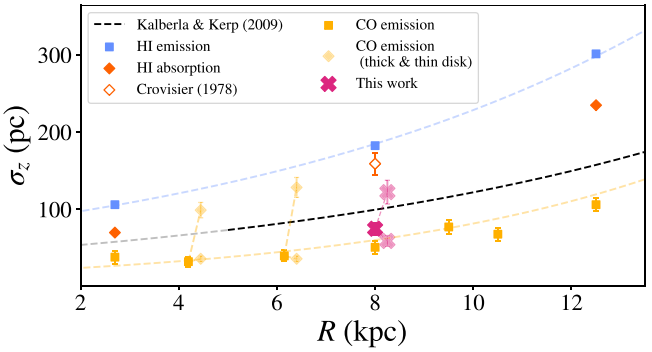

Figure 6. A re-creation of Figure 11 of N. M. McClure-Griffiths et al. (2023), with new estimates of σ_z derived in this work overplotted. Yellow squares indicate the thickness of the molecular gas disk derived from observations of CO in emission (see Figure 6 in M. Heyer & T. M. Dame 2015, and references therein). For the Galactocentric radii probed by Y. Su et al. (2021), we separate σ_z into the thick and thin components using dashed lines, with semitransparent yellow squares indicating σ_z for the molecular thin and thick disks. Orange diamonds indicate the thickness of the cold H I disk derived from observations of H I in absorption (J. M. Dickey et al. 2009, 2022). The solar neighborhood estimate for the cold H I disk from J. Crovisier (1978) used by N. M. McClure-Griffiths et al. (2023) is shown as an open orange diamond. Blue squares indicate the thickness of the total H I disk derived from observations of H I in emission (HI4PI Collaboration et al. 2016). Estimates from this work (in the solar neighborhood; Table 1) are shown as magenta crosses. The result for the full $|b| > 5°$ sample is shown as an opaque cross. We then separate σ_z for cold H I in the solar neighborhood into the thin and thick components (corresponding to results for the $\tau > 0.1$ and $\tau < 0.1$ samples; Table 1) using dashed lines, with semitransparent crosses indicating σ_z for these two samples. A black dashed line shows the exponential fit to the H I disk thickness from P. M. W. Kalberla & J. Kerp (2009), valid for Galactocentric radii 5 kpc $\lesssim R \lesssim$ 35 kpc (a gray dashed line shows the extrapolated fit for $R < 5$ kpc). Yellow and blue dashed lines show our exponential fits to the disk thickness determined from H I emission and CO emission, respectively.

CNM data are sparse and that our methods are different from those used by J. M. Dickey et al. (2009, 2022), so future work will be needed to more definitively characterize the radial structure of the CNM.

More work is needed to understand the connection between the thin and thick disks measured in CO and the thin and thick disks inferred here for the optically thicker and optically thinner H I, respectively. Direct comparisons of H I absorption to molecular line observations have been extremely limited owing to the relatively small number of sight lines where H I absorption has been measured (e.g., H. Nguyen et al. 2019; D. R. Rybarczyk et al. 2022; A. Hafner et al. 2023; G. Park et al. 2023). Moreover, observations of the thick molecular gas have probed Galactocentric radii less than $R_\odot$ (derived by observing gas at tangent points in the first quadrant; S. Malhotra 1994; T. M. Dame & P. Thaddeus 1994; Y. Su et al. 2021), whereas our observations probe the solar neighborhood (see Figure 6). Nevertheless, the intriguing similarity may suggest that cold H I and molecular gas are well mixed.

4.2. The Velocity Dispersion of Cold H I

Both observations and models of the vertical structure of the atomic ISM suggest that the vertical pressure balance is maintained through turbulence (e.g., F. J. Lockman & C. S. Gehman 1991; H. Koyama & E. C. Ostriker 2009). The varying velocity dispersions[6] of gas in discrete ISM phases contribute to the differences in vertical structure between phases, so quantifying the velocity dispersion of the CNM is important for constraining models of the multiphase structure of galaxies (e.g., C. A. Narayan & C. J. Jog 2002).

[6] In this work, we use "velocity dispersion" to refer to the cloud-to-cloud velocity dispersion, not the velocity dispersion within a single H I cloud.

Table 2
Estimates of σ_v from the `kinematic_scaleheight` Code for Different Samples of BIGHICAT Components

Sample	N	$\sigma_{v,\mathrm{ls}}$ (km s^{-1})	$\sigma_{v,\mathrm{MR}}$ (km s^{-1})	$\sigma_{v,\mathrm{shape}}$ (km s^{-1})
$\lvert b\rvert > 5°$	768	11.7 ± 0.3	6.5 ± 0.3	6.5 ± 0.4
$\tau > 0.1$, $\lvert b\rvert > 5°$	431	8.5 ± 0.3	5.8 ± 0.4	5.8 ± 0.4
$\tau < 0.1$, $\lvert b\rvert > 5°$	336	14.3 ± 0.6	7.5 ± 0.9	7.5 ± 0.9
$N(\mathrm{HI}) > 10^{19.5}$ cm^{-2}, $\lvert b\rvert > 5°$	429	9.0 ± 0.3	5.5 ± 0.3	5.5 ± 0.3
$N(\mathrm{HI}) < 10^{19.5}$ cm^{-2}, $\lvert b\rvert > 5°$	216	14.1 ± 0.7	8.5 ± 1.0	8.5 ± 1.0
$T_s < 80$ K, $\lvert b\rvert > 5°$	423	12.0 ± 0.4	6.4 ± 0.4	6.4 ± 0.4
$T_s > 80$ K, $\lvert b\rvert > 5°$	257	10.2 ± 0.4	5.8 ± 0.5	5.8 ± 0.5
$T_s < 80$ K, $\tau > 0.1$, $\lvert b\rvert > 5°$	296	8.8 ± 0.4	5.1 ± 0.4	5.1 ± 0.4
$T_s > 80$ K, $\tau < 0.1$, $\lvert b\rvert > 5°$	171	11.2 ± 0.6	6.2 ± 0.7	6.2 ± 0.7

Note. The first column describes each subsample. The second column lists the number of unique BIGHICAT components, N, belonging to each subsample. The third column lists the velocity dispersion derived using the `kinematic_scaleheight` least-squares method, $\sigma_{v,\mathrm{ls}}$. The fourth column lists the velocity dispersion derived using the `kinematic_scaleheight` moment ratio method, $\sigma_{v,\mathrm{MR}}$. The fifth column lists the velocity dispersion derived using the `kinematic_scaleheight` shape method, $\sigma_{v,\mathrm{shape}}$.

Table 2 lists the velocity dispersions, σ_v, inferred from the four fitting methods implemented by `kinematic_scaleheight` for the same BIGHICAT subsamples discussed in Table 1. The estimates for the least-squares methods are systematically higher than those from the two MCMC methods. This is unsurprising given that the MCMC methods filter out outliers while the least-squares method does not. We quote errors for the least-squares methods using $\sigma_v/\sqrt{2N}$ to be consistent with J. Crovisier (1978). Errors for the MCMC methods are determined using a Bayesian approach (T. V. Wenger et al. 2024).

For the samples in Tables 1 and 2, we derive $\sigma_v \sim 5$–8.5 km s^{-1}. N. M. McClure-Griffiths & J. M. Dickey (2007) investigated the kinematics of H I observed in emission by the Southern Galactic Plane Survey. They found that H I peculiar velocities were characterized by three components: a cold component with $\sigma_v = 6.3$ km s^{-1}, a warmer component with $\sigma_v = 12.3$ km s^{-1}, and a component with $\sigma_v = 25.9$ km s^{-1} (note that "cold" and "warm" here refer to the kinematics, not necessarily the actual temperature of the gas). Previously, F. J. Lockman & C. S. Gehman (1991) derived a similar three-component fit for H I emission at high latitudes. The velocity dispersions we report in Table 2 are consistent with the kinematically cold component identified in H I emission observations. This consistency likely suggests that the component measured in emission is indeed tracing the CNM, which affirms that, at least in some cases, H I emission can be used as a reliable tracer of the full multiphase atomic gas rather than just the warmer H I (e.g., K. Takakubo 1967; U. Mebold 1972; U. Haud & P. M. W. Kalberla 2007; A. Marchal et al. 2019).

As in Table 1, we see differences in Table 2 between the results for optically thicker and higher column density samples —the samples with $\tau > 0.1$ or $N(\mathrm{H\,I}) > 10^{19.5}$ cm^{-2} have velocity dispersions $\sim$5.5 km s^{-1}, whereas the samples with $\tau < 0.1$ or $N(\mathrm{H\,I}) < 10^{19.5}$ cm^{-2} have velocity dispersions $\sim$8 km s^{-1}. We note that the velocity dispersions measured for lower optical depth / lower column density subsamples are still

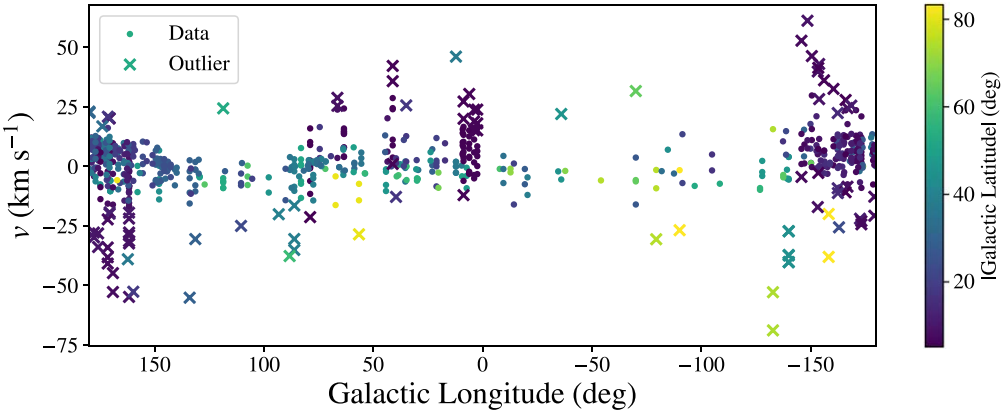

Figure 7. ℓ–v diagram of all 768 components in the BIGHICAT with $|b| > 5°$. Data are shown as filled circles. Outliers are shown as crosses. The color of each marker corresponds to the absolute value of the Galactic latitude of that component.

in the range expected for CNM and lower than those expected for the WNM (e.g., N. M. McClure-Griffiths & J. M. Dickey 2007; C. E. Murray et al. 2018). The trend in σ_v follows that observed in σ_z, with lower velocity dispersions inferred for samples of clouds with higher optical depths. This is consistent with the idea that the vertical balance of the cold gas is indeed maintained primarily by turbulence (F. J. Lockman & C. S. Gehman 1991; H. Koyama & E. C. Ostriker 2009).

4.3. Constraints on the Solar Motion

Besides measuring the vertical thickness and velocity dispersion of the cold H I, the methods employed in the `kinematic_scaleheight` code also constrain the solar peculiar velocity components, which characterize the Sun's motion relative to the LSR in the direction of the Galactic center ($U_\odot$), in the direction of rotation ($V_\odot$), and in the direction of the Galactic north pole ($W_\odot$). For the full sample of BIGHICAT features at $|b| > 5°$, we find $(U_\odot, V_\odot, W_\odot) = (12.9 \pm 0.4, 15.1 \pm 0.7, 8.8 \pm 0.5)$ km s^{-1}. The results for the moment ratio and shape methods are nearly identical. Moreover, all of the samples in Table 1 have $U_\odot$, $V_\odot$, and $W_\odot$ values consistent with the results for the full sample. There is significant variation in the $U_\odot$, $V_\odot$, and $W_\odot$ values for different samples when estimated using the least-squares approach. This is understandable given that the least-squares approach is not robust to outliers, which make up ∼10%–30% of each of the samples in Table 1.

In recent years, a variety of techniques have been used to estimate the Sun's peculiar motion (see Table 1 of P.-J. Ding et al. 2019 for a summary of results). Our estimates of $U_\odot$, $V_\odot$, and $W_\odot$ agree reasonably well (within $\lesssim 3\sigma$) with some estimates derived from stellar kinematics (R. Schonrich et al. 2010; C. Francis 2013; C. Francis & E. Anderson 2014; O. Zbinden & P. Saha 2019) and Galactic rotation models based on parallaxes (M. J. Reid et al. 2014, 2019). Nevertheless, estimates of $U_\odot$, $V_\odot$, and $W_\odot$ vary considerably depending on the observational sample and the method used, and our results are inconsistent with some measurements derived from stellar kinematics (P.-J. Ding et al. 2019, and references therein).

4.4. Inspection of Outliers

While we are primarily concerned with constraining the thickness of the cold atomic gas disk in the Milky Way, the identification of outliers in the Bayesian models developed by T. V. Wenger et al. (2024) allows us to investigate CNM structures that exist outside the standard kinematic and/or structural distribution. Outliers are identified as structures whose positions in (ℓ, b, v) space are inconsistent with our model of local gas clouds following circular Galactic rotation. Such structures could potentially trace dynamical events and inform our understanding of the formation and survival of the CNM in different environments. In most of the samples we consider, ∼20% of H I structures are categorized as outliers. Figure 7 shows the longitude–velocity (ℓ–v) diagram for all the features in the $|b| > 5°$ sample. The outliers are shown as crosses, and the nonoutliers are shown as filled circles. Point are colored according to Galactic latitude.

In Figure 8, we show that many of the outliers in the outer Galaxy are associated with the Outer Arm (e.g., L. G. Hou & J. L. Han 2014). If we make a reasonable assumption about the disk thickness—say, $\sigma_z \lesssim 150$ pc (J. M. Dickey et al. 2022; T. V. Wenger et al. 2024)—then our latitude cut, $|b| > 5°$, ensures that a majority of the H I structures in our sample are at a distance <1 kpc and virtually all of them are at a distance <2 kpc. However, if the H I disk in the outer Galaxy is warped (J. Binney 1992, and references therein) or flared (P. M. W. Kalberla & J. Kerp 2009, and references therein), then our latitude criterion may not be sufficient to filter out features in the outer disk. Indeed, it is well established that H I toward the outer Galaxy (including the Outer Arm) is warped and flared (e.g., E. S. Levine et al. 2006; P. M. W. Kalberla & L. Dedes 2008), so it is not surprising to have Outer Arm features interloping on our local H I sample. Given that all of the features that are clearly associated with the Outer Arm are flagged as outliers, we still consider $|b| > 5°$ as a reasonable criterion for selecting local gas when using the Bayesian models from T. V. Wenger et al. (2024). On the other hand, for the least-squares method, which does not remove such outliers, a more stringent latitude cut is probably necessary to circumvent the features from the warped/flared outer Galaxy at intermediate latitudes.

Still, some of outlying components in Figure 7 indeed appear to trace local gas. Some outliers in the first quadrant have low latitudes, very likely tracing more distant gas structures (which are inconsistent with our model of the CNM at $d \lesssim 2$ kpc). Meanwhile, other outliers have both high latitudes (indicating that they are likely nearby) and high velocities. All of the velocities in the BIGHICAT sample are less than 62 km s^{-1}, so the nearby outlying features do not represent high-velocity

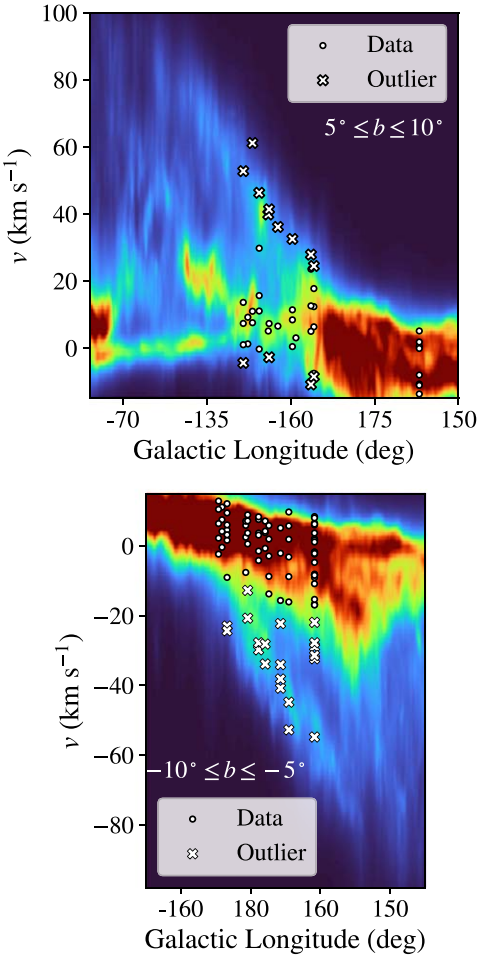

Figure 8. ℓ–v diagram showing components associated with flared/warped H I in the outer Galaxy, associated with the Outer Arm (E. S. Levine et al. 2006; P. M. W. Kalberla & L. Dedes 2008). White crosses indicate points identified as outliers. White circles are the nonoutlying components. The background map shows the H I emission from HI4PI (HI4PI Collaboration et al. 2016), integrated over $5^\circ \leqslant b \leqslant 10^\circ$ (top) and $-10^\circ \leqslant b \leqslant -5^\circ$ (bottom).

clouds ($|v| > 90\,\mathrm{km\,s^{-1}}$; B. P. Wakker & H. van Woerden 1997), but they may represent intermediate-velocity clouds (IVCs). To characterize these gas structures—and perhaps better understand the origin of IVCs—we try to identify counterparts in H I emission and 3D space. In Figure 9, we present maps of H I emission (top panel, contours) and dust emission (top panel, background) associated with six components that are identified as outliers. These six components were selected based on two criteria: (1) we were able to identify H I emission that was spatially and kinematically associated with the H I absorption, and (2) we were further able to connect the H I emission structures to structures in the recent three-dimensional map of the ISM constructed by G. Edenhofer et al. (2024).

To illustrate the association between these six H I absorption components and the H I emission, we also show ℓ–v diagrams of the H I emission in these directions (middle panels in Figure 9). As before, the BIGHICAT features flagged as outliers are overlaid as crosses, and features not flagged as outliers are overlaid as circles. We isolate the H I emission at velocities associated with the outlying components (outlined by horizontal dashed lines in the ℓ–v diagrams). The emission at these velocities is shown in the white contours in the top panels of Figure 9. We then identified structures in the G. Edenhofer et al. (2024) dust maps that showed a similar morphology to the H I emission (the background images in the top panels of Figure 9, identified by eye). In the bottom panels of Figure 9, we also show longitude–distance (ℓ–d) diagrams (similar to the ℓ–v diagram, but the y-axis is a third spatial dimension, rather than a spectral one) in these directions. We use horizontal dashed lines to show the distances to the dust structures that appear to be associated with the structures identified in H I emission. In this way, we characterized the kinematics and morphology of H I emission and 3D density structures of a selection of outlying components.

Five of the six components (illustrated in the first five panels in Figure 9, in the directions of 3C 454.3, J0834+555, 4C +25.14, J1638+625, and J1351–148) appear to be associated with extended arc-like features. The structure in the direction of 4C+25.14 appears to be associated with the Local Bubble wall (T. J. O'Neill et al. 2024). The H I emission in the direction of J1351–148 at $\sim$20–40 km s^{-1} is associated with the Local Bubble wall (clear in the ℓ–d diagram; T. J. O'Neill et al. 2024 report a distance to the Local Bubble wall of 107 pc in this direction), as well as an extended structure at a distance of $\sim$110–160 pc on the eastern side (see the ℓ–d diagram at $-60^\circ \lesssim \ell \lesssim -40^\circ$). While both of these components contribute to the H I emission at these velocities, at the longitude of J1351–148 it appears that only the nearer structure (i.e., Local Bubble wall) is present, so we conclude that this outlying component is associated with the Local Bubble wall. The other four structures shown in Figure 7 are not associated with the Local Bubble wall but are instead associated with discrete structures 400–600 pc from the Sun.

The analysis here remains limited, but future work connecting cold H I structures at anomalous velocities (perhaps representing IVCs) with the 3D dust maps in a more systematic way (see, e.g., J. D. Soler et al. 2023) could help establish the origin of these cold gas structures. For example, here we find that two CNM clouds with anomalous velocities are associated with the Local Bubble wall (B. Y. Welsh et al. 2004). More broadly, such comparisons could also help illuminate the structure of the CNM and its relation to the disk–halo interface (F. J. Lockman 2002; S. Stanimirović et al. 2006).

5. Discussion

Consistent with T. V. Wenger et al. (2024), we find that the vertical thickness of the CNM in the solar neighborhood, σ_z, is significantly smaller than previously reported (J. Crovisier 1978; P. Belfort & J. Crovisier 1984; J. M. Dickey et al. 2022). We further find that the derived thickness depends strongly on the physical properties of the H I structures considered—H I structures with optical depths $\gtrsim$0.1 and/or column densities $\gtrsim 10^{20}\,\mathrm{cm^{-2}}$ are characterized by a scale height $\sigma_z \approx$ 50–60 pc, while H I structures with optical depths $\lesssim$0.1 and/or column densities $\lesssim 10^{20}\,\mathrm{cm^{-2}}$ are characterized by a scale height $\sigma_z \approx$ 100–120 pc. It is worth noting here that the sensitivity of the J. Crovisier et al. (1978) H I absorption survey means that J. Crovisier (1978) was considering primarily structures with $\tau \gtrsim 0.1$. Thanks to improvements in sensitivity over the past half century, approximately half of the structures in the BIGHICAT would not have been detectable by J. Crovisier et al. (1978) and so would not have been included in the sample of J. Crovisier (1978).

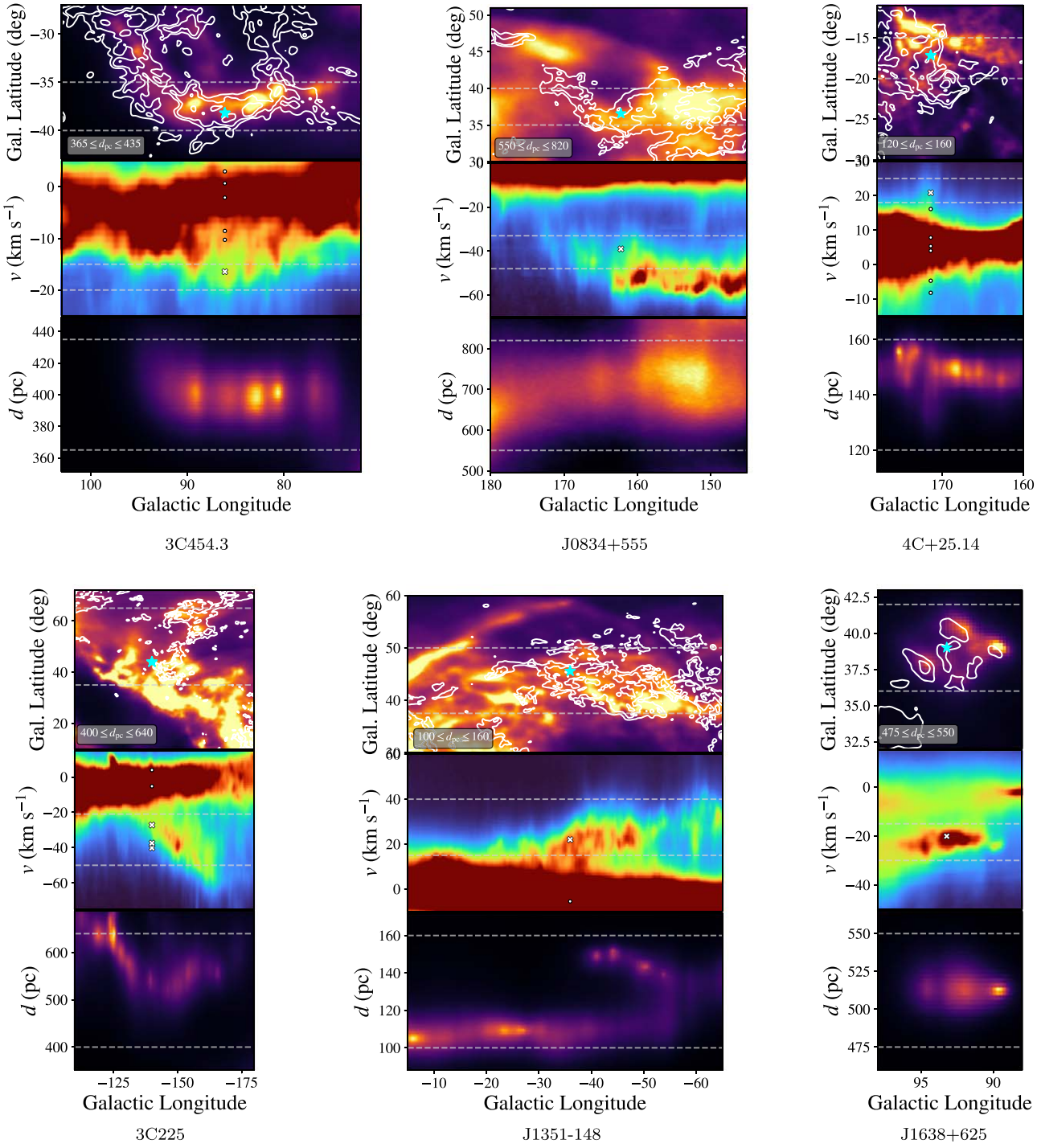

Figure 9. Maps of gas associated with six outlying CNM components. Top panels:H I emission (white contours) overlaid on maps of dust emission. H I emission is integrated over the velocity intervals shown with horizontal dashed lines in the middle panels. Dust emission is integrated over the distance intervals shown with horizontal dashed lines in the bottom panels. Middle panels: ℓ–v diagrams of H I emission from HI4PI (HI4PI Collaboration et al. 2016). Outlying components are shown with white crosses, while nonoutlying components are shown as white circles. The H i emission is integrated over the latitude intervals shown with horizontal lines in the top panels. Bottom panels: ℓ–d diagrams from the G. Edenhofer et al. (2024) data cube. The dust emission is integrated over the latitude intervals shown with horizontal lines in the top panels.

The results presented here challenge the idea that the CNM thickness increases monotonically (with local variations) with Galactocentric radius (e.g., P. M. W. Kalberla & L. Dedes 2008; J. M. Dickey et al. 2022; N. M. McClure-Griffiths et al. 2023). Instead, they imply that the thickness of the CNM is roughly the same at the solar circle as in the inner Galaxy, at least for $\tau \gtrsim 0.1$.

Recently, R. J. Smith et al. (2023) investigated the CNM distribution at high resolution (physical scales $\lesssim$1 pc) in a simulation of an isolated spiral galaxy (updated from R. G. Tress et al. 2020, 2021). They showed that the thickness of the CNM was systematically narrower than that of the total H I (CNM+WNM) and was roughly constant across most of the disk (excluding the center, where σ_z was smaller), with

$\sigma_z \sim 100$ pc. While the value of σ_z measured for the CNM was mostly stable, significant (∼factor of two) local variations did appear in some parts of the galaxy. They considered both a constant radiation field and a radially decreasing radiation field; the radial extent of the CNM changed between the two models, but the vertical distribution of the CNM was similar (and similarly flat with galactocentric radius) in both models. Their results are consistent with the picture developed in this work, where the vertical thickness of the CNM in the solar neighborhood is similar to that in the inner Galaxy (J. M. Dickey et al. 2022) (compare Figures 6–10 of R. J. Smith et al. 2023).

The vertical equilibrium of the CNM is set by the balance of gravity and the pressure gradient. In the CNM, it is thought that the turbulent pressure alone may be sufficient to sustain the vertical equilibrium (F. J. Lockman & C. S. Gehman 1991; H. Koyama & E. C. Ostriker 2009); the thermal pressure is minimal for such cold gas but more important for warmer ISM components (e.g., C.-G. Kim & E. C. Ostriker 2015). Indeed, in both observations and simulations of galaxies, the pressure of the cold atomic ISM is dominated by dynamical processes (C.-G. Kim & E. C. Ostriker 2015; R. Herrera-Camus et al. 2017). While our results imply a thinner CNM disk than reported by some previous experiments (J. Crovisier 1978; P. Belfort & J. Crovisier 1984; F. J. Lockman & C. S. Gehman 1991; J. M. Dickey et al. 2022), Table 2 also shows that the Bayesian models from T. V. Wenger et al. (2024) infer relatively small velocity dispersions (see the two rightmost columns). For example, the velocity dispersions in Table 2 are about a factor of two smaller than those measured by F. J. Lockman & C. S. Gehman (1991) from H I emission. The scale heights in Table 1 are also about a factor of two smaller than those inferred by F. J. Lockman & C. S. Gehman (1991), so despite our updated estimates of σ_z and σ_v, it remains plausible that the vertical support of the CNM can still be explained by turbulence.

The CNM precedes the formation of molecular clouds (e.g., P. F. Goldsmith et al. 2007; S. Stanimirović et al. 2014), so the structure of the CNM influences the structure of the molecular gas disk. The molecular gas traced by CO in the Milky Way is known to be organized in a thin disk, $\sigma_z \sim 40$ pc, and a thick disk, $\sigma_z \sim 120$ pc (T. M. Dame & P. Thaddeus 1994; S. Malhotra 1994; Y. Su et al. 2021). In Figure 6, estimates for the total molecular gas disk are shown as opaque yellow squares (see Figure 6 of M. Heyer & T. M. Dame 2015, and references therein), while estimates for the thin and thick components are shown as semitransparent yellow squares (Y. Su et al. 2021). The thickness of the thin disk is similar to our estimate for the H I structures with $\tau > 0.1$ (especially if we only consider those with $T_S < 80$ K; see Table 1). The similarity of the vertical thickness of the molecular gas disk with the vertical thickness we find for cold, optically thick H I is consistent with recent work that suggests that only this H I contributes significantly to the formation of molecular clouds (S. Stanimirović et al. 2014; H. Nguyen et al. 2019; D. R. Rybarczyk et al. 2022; A. Hafner et al. 2023; G. Park et al. 2023). The connection is particularly striking because we find that the H I in this thin disk has $\tau \gtrsim 0.1$ and $N(\mathrm{H\,I}) \gtrsim 10^{20}$ cm^{-2}, which are roughly the same criteria that have been deemed necessary for the formation of molecular gas (D. R. Rybarczyk et al. 2022; A. Hafner et al. 2023; G. Park et al. 2023). It is also worth noting that the thickness of the molecular gas disk has been shown to be roughly constant with Galactocentric radius from $R \sim 3$ kpc out to the solar circle (M. Heyer & T. M. Dame 2015, and references therein), consistent with the trend that Figure 6 suggests exists for cold, optically thick H I.

Meanwhile, the thickness of the thick molecular disk, $\sigma_z \sim 120$ pc, is similar to our estimate for the thickness of the atomic gas disk for absorbing H I structures with $\tau < 0.1$ (see Figure 6). Recently, D. R. Rybarczyk et al. (2022) identified diffuse molecular gas (traced by HCO^+ absorption) associated with the CNM at optical depths <0.1. The spectral signature of this diffuse gas bore striking resemblance to a signature identified in OH emission by M. P. Busch et al. (2021), who showed that this diffuse gas belonged to a thick disk (they used a very simple cylindrical model with a thickness of 200 pc). The similarity between our measurement of the optically thinner CNM and the thick molecular disk (T. M. Dame & P. Thaddeus 1994; S. Malhotra 1994; Y. Su et al. 2021), as well as the recent detection of diffuse molecular gas associated with this H I, could indicate that some of the molecular gas and the cold atomic gas at higher z share a common origin.

6. Conclusions

We present new estimates of the vertical thickness of the cold atomic gas disk in the solar neighborhood. We apply the `kinematic_scaleheight` code (T. V. Wenger 2024; T. V. Wenger et al. 2024), which uses four methods—including the method developed by J. Crovisier (1978)—to estimate the vertical thickness of the disk from a given sample of absorbing structures, to subsamples of the BIGHICAT. We focus only on H I structures at Galactic latitudes $|b| > 5°$, where most of the gas along the line of sight is local ($d < 2$ kpc).

As discussed in T. V. Wenger et al. (2024), the three new approaches to measure the vertical thickness of the CNM disk in the solar neighborhood have corrected the J. Crovisier (1978) approach and lead to a smaller disk height than previously reported (J. Crovisier 1978; P. Belfort & J. Crovisier 1984; J. M. Dickey et al. 2022). In fact, the values of σ_z that we measure for different samples of local H I structures (Table 1) are similar to those measured in the inner Galaxy, at $R \sim 3$ kpc (J. M. Dickey et al. 2022). This challenges the conventional picture of a vertical thickness that gradually rises with Galactocentric radius (N. M. McClure-Griffiths et al. 2023, see Figure 6). Instead, this is more in line with recent simulations of the multiphase ISM (R. J. Smith et al. 2023) that have found that the CNM thickness is roughly constant with galactocentric radius, from just outside the galactic center out to the outer galaxy (although they do not find CNM at very large galactic radii, as measured in observations of the Milky Way from J. M. Dickey et al. 2009).

If we consider the entire BIGHICAT sample at $|b| > 5°$, we find $\sigma_z \approx 75 \pm 8$ pc (assuming a Gaussian shape to the vertical distribution). However, if we divide the high-latitude BIGHICAT into an optically thicker sample ($\tau > 0.1$) and an optically thinner sample ($\tau < 0.1$), we find that the optically thicker sample has a significantly narrower vertical distribution than the optically thicker sample, with $\sigma_z \approx 60$ and 120 pc, respectively. We find similar results if we separate by column density (with a boundary of $N(\mathrm{H\,I}) \sim 10^{20}$) instead of optical depth. This is noteworthy because $\tau \approx 0.1$ and $N(\mathrm{H\,I}) \approx 10^{19.5}$ have been shown to be necessary (but not sufficient) prerequisites for molecule formation in the diffuse ISM. The thicknesses we derive for the optically thicker or higher column

density samples, $\sigma_z \sim 50$–60 pc, are consistent with estimates for the thickness of the molecular gas disk in the solar neighborhood (e.g., D. B. Sanders et al. 1984; D. A. Grabelsky et al. 1987; L. Bronfman et al. 1988; D. P. Clemens et al. 1988; S. Malhotra 1994; H. Nakanishi & Y. Sofue 2006). Our results are consistent with the interpretation that optically thick, high column density CNM gas leads to the formation of molecular clouds (e.g., S. Stanimirović et al. 2014).

Nevertheless, we do not find significant variations in the disk thickness as a function of H I spin temperature (approximately equal to the gas kinetic temperature in these environments). However, A. S. Hill et al. (2018) showed that, in 3D magnetohydrodynamic simulations of the multiphase ISM (M. K. R. Joung & M.-M. Mac Low 2006; M. R. Joung et al. 2009; A. S. Hill et al. 2012), the distribution of gas at temperatures $\lesssim$200 K was relatively uniform for $|z| \lesssim 100$ pc. A total of 89% of the components in our high-latitude BIGHICAT sample have $T_S < 200$ K. Variations in the scale height as a function of temperature are thought to manifest over much larger temperature ranges than considered here (see Figure 6 of A. S. Hill et al. 2018).

For each sample of H I structures we inspect, we estimate both the vertical thickness of the cold disk, σ_z, and the cloud-to-cloud velocity dispersion, σ_v. The velocity dispersions are reported in Table 2, ranging from 5.1 to 8.5 km s^{-1}. These velocity dispersions are significantly lower than those inferred using the original technique implemented by J. Crovisier (1978) (see the third column of Table 2), as well as that which F. J. Lockman & C. S. Gehman (1991) inferred from H I emission to estimate the thickness of the cold disk. Yet, as shown in Table 1, our estimates of the disk thickness are also lower. If we make a reasonable estimate of the gravitational potential close to the plane (e.g., K. Kuijken & G. Gilmore 1989, as discussed by F. J. Lockman & C. S. Gehman 1991), then we find that the inferred velocity dispersions (Table 2) and the inferred scale heights (Table 1) remain consistent with the vertical balance of the CNM being maintained primarily by turbulence (F. J. Lockman & C. S. Gehman 1991; H. Koyama & E. C. Ostriker 2009).

Besides measuring the vertical distribution and velocity dispersion of cold H I, we are also able to constrain the solar motion with respect to the LSR. For the full high-latitude BIGHICAT sample, we find $(U_\odot,\ V_\odot,\ W_\odot) = (12.9 \pm 0.4,\ 15.1 \pm 0.7,\ 8.8 \pm 0.5)$ km s^{-1}, consistent with estimates derived from stellar kinematics (R. Schonrich et al. 2010; C. Francis 2013; C. Francis & E. Anderson 2014; O. Zbinden & P. Saha 2019) and Galactic rotation models based on parallaxes (M. J. Reid et al. 2014, 2019) (although estimates of $U_\odot$, $V_\odot$, and $W_\odot$ depend on both the observational sample and the method used, and our results are inconsistent with some other measurements; P.-J. Ding et al. 2019, and references therein).

We also identify outliers that are not well fit by the simple Galactic rotation model; some of these outliers may represent IVCs. In Section 4.4, we show that several of these outlying components are associated with extended arc-like structures. Further, the recent emergence of 3D maps of the local ISM (e.g., G. M. Green et al. 2019; R. Lallement et al. 2019; R. H. Leike et al. 2020; G. Edenhofer et al. 2024) has made it possible to map the 3D spatial position and morphology of gas structures identified in two spatial dimensions using spectral data cubes (see, e.g., J. D. Soler et al. 2023). Here we find that two of the cold H I outliers are very likely associated with the Local Bubble wall (T. J. O'Neill et al. 2024).

Acknowledgments

This research has made use of NASA's Astrophysics Data System Bibliographic Services. D.R.R. is supported by a National Science Foundation Astronomy and Astrophysics Postdoctoral Fellowship under award AST-2303902. T.V.W. is supported by a National Science Foundation Astronomy and Astrophysics Postdoctoral Fellowship under award AST-2202340. The authors acknowledge Interstellar Institute's program "II6" and the Paris-Saclay University's Institut Pascal for hosting discussions that nourished the development of the ideas behind this work. We would also like to thank N. M. McClure-Griffiths, R. Benjamin, and J. M. Dickey for useful discussions regarding the content of this paper.

Software: Astropy (Astropy Collaboration et al. 2013), `kinematic_scalehieght` (T. V. Wenger 2024).

ORCID iDs

Daniel R. Rybarczyk https://orcid.org/0000-0003-3351-6831
Trey V. Wenger https://orcid.org/0000-0003-0640-7787
Snežana Stanimirović https://orcid.org/0000-0002-3418-7817

References

Astropy Collaboration, Robitaille, T. P., Tollerud, E. J., et al. 2013, A&A, 558, A33
Belfort, P., & Crovisier, J. 1984, A&A, 136, 368
Binney, J. 1992, ARA&A, 30, 51
Bloemen, J. B. G. M. 1987, ApJ, 322, 694
Boulares, A., & Cox, D. P. 1990, ApJ, 365, 544
Bronfman, L., Cohen, R. S., Alvarez, H., May, J., & Thaddeus, P. 1988, ApJ, 324, 248
Busch, M. P., Engelke, P. D., Allen, R. J., & Hogg, D. E. 2021, ApJ, 914, 72
Clemens, D. P., Sanders, D. B., & Scoville, N. Z. 1988, ApJ, 327, 139
Crovisier, J. 1978, A&A, 70, 43
Crovisier, J., Kazes, I., & Aubry, D. 1978, A&AS, 32, 205
Dame, T. M., & Thaddeus, P. 1994, ApJL, 436, L173
Dénes, H., McClure-Griffiths, N. M., Dickey, J. M., Dawson, J. R., & Murray, C. E. 2018, MNRAS, 479, 1465
Dickey, J. M., Dempsey, J. M., Pingel, N. M., et al. 2022, ApJ, 926, 186
Dickey, J. M., & Lockman, F. J. 1990, ARA&A, 28, 215
Dickey, J. M., Strasser, S., Gaensler, B. M., et al. 2009, ApJ, 693, 1250
Ding, P.-J., Zhu, Z., & Liu, J.-C. 2019, RAA, 19, 068
Edenhofer, G., Zucker, C., Frank, P., et al. 2024, A&A, 685, A82
Falgarone, E., & Lequeux, J. 1973, A&A, 25, 253
Francis, C. 2013, MNRAS, 436, 1343
Francis, C., & Anderson, E. 2014, CeMDA, 118, 399
Goldsmith, P. F., Li, D., & Krčo, M. 2007, ApJ, 654, 273
Grabelsky, D. A., Cohen, R. S., Bronfman, L., Thaddeus, P., & May, J. 1987, ApJ, 315, 122
Green, G. M., Schlafly, E., Zucker, C., Speagle, J. S., & Finkbeiner, D. 2019, ApJ, 887, 93
Hafner, A., Dawson, J. R., Nguyen, H., et al. 2023, PASA, 40, e015
Haud, U., & Kalberla, P. M. W. 2007, A&A, 466, 555
Heiles, C., & Troland, T. H. 2003a, ApJ, 586, 1067
Heiles, C., & Troland, T. H. 2003b, ApJS, 145, 329
Herrera-Camus, R., Bolatto, A., Wolfire, M., et al. 2017, ApJ, 835, 201
Heyer, M., & Dame, T. M. 2015, ARA&A, 53, 583
HI4PI Collaboration, Ben Bekhti, N., Flöer, L., et al. 2016, A&A, 594, A116
Hill, A. S., Joung, M. R., Mac Low, M.-M., et al. 2012, ApJ, 750, 104
Hill, A. S., Mac Low, M.-M., Gatto, A., & Ibáñez-Mejía, J. C. 2018, ApJ, 862, 55
Hotan, A. W., Bunton, J. D., Chippendale, A. P., et al. 2021, PASA, 38, e009
Hou, L. G., & Han, J. L. 2014, A&A, 569, A125
Joung, M. K. R., & Mac Low, M.-M. 2006, ApJ, 653, 1266

Joung, M. R., Mac Low, M.-M., & Bryan, G. L. 2009, ApJ, 704, 137
Kalberla, P. M. W., & Dedes, L. 2008, A&A, 487, 951
Kalberla, P. M. W., Dedes, L., Kerp, J., & Haud, U. 2007, A&A, 469, 511
Kalberla, P. M. W., & Kerp, J. 2009, ARA&A, 47, 27
Kim, C.-G., & Ostriker, E. C. 2015, ApJ, 815, 67
Koyama, H., & Ostriker, E. C. 2009, ApJ, 693, 1346
Kuijken, K., & Gilmore, G. 1989, MNRAS, 239, 605
Lallement, R., Babusiaux, C., Vergely, J. L., et al. 2019, A&A, 625, A135
Leike, R. H., Glatzle, M., & Enßlin, T. A. 2020, A&A, 639, A138
Levine, E. S., Blitz, L., & Heiles, C. 2006, ApJ, 643, 881
Lockman, F. J. 2002, ApJL, 580, L47
Lockman, F. J., & Gehman, C. S. 1991, ApJ, 382, 182
Lockman, F. J., Jahoda, K., & McCammon, D. 1986, ApJ, 302, 432
Malhotra, S. 1994, ApJ, 433, 687
Marasco, A., & Fraternali, F. 2011, A&A, 525, A134
Marasco, A., Fraternali, F., Heald, G., et al. 2019, A&A, 631, A50
Marchal, A., Miville-Deschênes, M.-A., Orieux, F., et al. 2019, A&A, 626, A101
McClure-Griffiths, N. M., & Dickey, J. M. 2007, ApJ, 671, 427
McClure-Griffiths, N. M., Dickey, J. M., Gaensler, B. M., et al. 2005, ApJS, 158, 178
McClure-Griffiths, N. M., Stanimirović, S., & Rybarczyk, D. R. 2023, ARA&A, 61, 19
McKee, C. F., & Ostriker, J. P. 1977, ApJ, 218, 148
Mebold, U. 1972, A&A, 19, 13
Mohan, R., Dwarakanath, K. S., & Srinivasan, G. 2004a, JApA, 25, 143
Mohan, R., Dwarakanath, K. S., & Srinivasan, G. 2004b, JApA, 25, 185
Murray, C. E., Stanimirović, S., Goss, W. M., et al. 2015, ApJ, 804, 89
Murray, C. E., Stanimirović, S., Goss, W. M., et al. 2018, ApJS, 238, 14
Murray, C. E., Stanimirović, S., Heiles, C., et al. 2021, ApJS, 256, 37
Murray, C. E., Stanimirović, S., Kim, C.-G., et al. 2017, ApJ, 837, 55
Nakanishi, H., & Sofue, Y. 2006, PASJ, 58, 847
Narayan, C. A., & Jog, C. J. 2002, A&A, 394, 89
Nguyen, H., Dawson, J. R., Lee, M.-Y., et al. 2019, ApJ, 880, 141
O'Neill, T. J., Zucker, C., Goodman, A. A., & Edenhofer, G. 2024, arXiv:2403.04961
Park, G., Lee, M.-Y., Bialy, S., et al. 2023, ApJ, 955, 145
Parker, E. N. 1969, SSRv, 9, 651
Reid, M. J., Menten, K. M., Brunthaler, A., et al. 2014, ApJ, 783, 130
Reid, M. J., Menten, K. M., Brunthaler, A., et al. 2019, ApJ, 885, 131
Rybarczyk, D. R., Stanimirović, S., Gong, M., et al. 2022, ApJ, 928, 79
Sanders, D. B., Solomon, P. M., & Scoville, N. Z. 1984, ApJ, 276, 182
Schonrich, R., Binney, J., & Dehnen, W. 2010, MNRAS, 403, 1829
Smith, R. J., Tress, R., Soler, J. D., et al. 2023, MNRAS, 524, 873
Soler, J. D., Zucker, C., Peek, J. E. G., et al. 2023, A&A, 675, A206
Stanimirović, S., Murray, C. E., Lee, M.-Y., Heiles, C., & Miller, J. 2014, ApJ, 793, 132
Stanimirović, S., Putman, M., Heiles, C., et al. 2006, ApJ, 653, 1210
Stil, J. M., Taylor, A. R., Dickey, J. M., et al. 2006, AJ, 132, 1158
Su, Y., Yang, J., Yan, Q.-Z., et al. 2021, ApJ, 910, 131
Takakubo, K. 1967, BAN, 19, 125
Taylor, A. R., Gibson, S. J., Peracaula, M., et al. 2003, AJ, 125, 3145
Tress, R. G., Smith, R. J., Sormani, M. C., et al. 2020, MNRAS, 492, 2973
Tress, R. G., Sormani, M. C., Smith, R. J., et al. 2021, MNRAS, 505, 5438
Vehtari, A., Gelman, A., Simpson, D., Carpenter, B., & Bürkner, P.-C. 2021, BayAn, 16, 667
Wakker, B. P., & van Woerden, H. 1997, ARA&A, 35, 217
Welsh, B. Y., Sallmen, S., & Lallement, R. 2004, A&A, 414, 261
Wenger, T. V. 2024, kinematic_scaleheight: Infer the vertical distribution of clouds in the solar neighborhood, Astrophysics Source Code Library, ascl:2403.003
Wenger, T. V., Rybarczyk, D. R., & Stanimirović, S. 2024, ApJ, 966, 206
Wolfire, M. G., McKee, C. F., Hollenbach, D., & Tielens, A. G. G. M. 2003, ApJ, 587, 278
Zbinden, O., & Saha, P. 2019, RNAAS, 3, 73